

EMBEDDED PROTOSTELLAR DISKS AROUND (SUB-)SOLAR PROTOSTARS. I. DISK STRUCTURE AND EVOLUTION

EDUARD I. VOROBYOV^{1,2}

accepted for publication by The Astrophysical Journal

ABSTRACT

We perform a comparative numerical hydrodynamics study of embedded protostellar disks formed as a result of the gravitational collapse of cloud cores of distinct mass ($M_{\text{cl}}=0.2\text{--}1.7 M_{\odot}$) and ratio of rotational to gravitational energy ($\beta=0.0028\text{--}0.023$). An increase in M_{cl} and/or β leads to the formation of protostellar disks that are more susceptible to gravitational instability. Disk fragmentation occurs in most models but its effect is often limited to the very early stage, with the fragments being either dispersed or driven onto the forming star during tens of orbital periods. Only cloud cores with high enough M_{cl} or β may eventually form wide-separation binary/multiple systems with low mass ratios and brown dwarf or sub-solar mass companions. It is feasible that such systems may eventually break up, giving birth to rogue brown dwarfs. Protostellar disks of *equal age* formed from cloud cores of greater mass (but equal β) are generally denser, hotter, larger, and more massive. On the other hand, protostellar disks formed from cloud cores of higher β (but equal M_{cl}) are generally thinner and colder but larger and more massive. In all models, the difference between the irradiation temperature and midplane temperature ΔT is small, except for the innermost regions of young disks, dense fragments, and disk's outer edge where ΔT is negative and may reach a factor of two or even more. Gravitationally unstable, embedded disks show radial pulsations, the amplitude of which increases along the line of increasing M_{cl} and β but tends to diminish as the envelope clears. We find that single stars with a disk-to-star mass ratio of order unity can be formed only from high- β cloud cores, but such massive disks are unstable and quickly fragment into binary/multiple systems. A substantial fraction of an embedded disk, especially its inner regions, spiral arms and dense clumps, may be optically thick, leading potentially to observational underestimates of disk masses in the embedded phase of star formation.

Subject headings: circumstellar matter — planetary systems: protoplanetary disks — hydrodynamics — ISM: clouds — stars: formation

1. INTRODUCTION

The early phases of the evolution of a protostellar disk, starting from its formation and ending with the clearing of a natal cloud core, determine the course along which a young stellar object (YSO) will evolve later in the T Tauri phase. Vigorous gravitational instability that develops in protostellar disks during the embedded phase of star formation (EPSF) serves to limit disk masses, effectively setting an upper limit on the mass accretion rates in the T Tauri phase and flattening the accretion rate–stellar mass relation for solar-type stars (Vorobyov & Basu 2009a). Disk fragmentation triggered by gas infall onto the disk from the collapsing cloud core could lead to the formation of giant planets or brown dwarfs, thus shaping the subsequent physical properties of stellar and planetary systems (e.g. Boley 2009; Boley et al. 2009; Machida et al. 2010; Vorobyov & Basu 2010a). The large spread in mass accretion rates inferred for embedded YSOs in Perseus, Serpens, and Ophiuchus star-forming regions by Enoch et al. (2009) can be accounted for by gravitational instability and fragmentation of protostellar disks in the EPSF (Vorobyov 2009b). In addition, episodic accretion caused by disk fragmentation (Vorobyov & Basu 2005,

2006, 2010b) can explain the observed luminosity spread in H-R diagrams of several-Myr-old star-forming regions (Baraffe et al. 2009) and resolve the long standing “luminosity problem” (Dunham et al. 2010), whereby protostars are underluminous compared to the accretion luminosity expected from analytical collapse calculations.

In spite of the pivotal role of the EPSF, our knowledge of protostellar disks in this phase is embarrassingly inadequate owing to difficulties with both observations and modeling. Observing this phase has been difficult because disks are only visible at wavelengths where resolution is poor. The added complication of the envelope structure in the embedded systems makes an extraction of disk parameters from interferometer data extraordinarily difficult with modern facilities. No wonder that most observations of disk properties have been focused on T Tauri disks (e.g. Akeson et al. 2002; Kitamura et al. 2002; Vicente & Alves 2005; Piétu et al. 2007; Andrews & Williams 2007; Andrews et al. 2009; Isella et al. 2009, and many others) and considerably fewer attempted studies of the embedded disks have been done so far (e.g. Andrews & Williams 2005; Eisner et al. 2005; Jørgensen et al. 2009).

Self-consistent numerical simulations of protostellar disks in the EPSF is no less difficult than observations due to vastly changing spatial and temporal scales involved. The matter is that it is not sufficient to just consider an *isolated* system with some presumed disk-to-star mass ratio. A self-consistent treatment of the inter-

¹ Institute for Computational Astrophysics, Saint Mary's University, Halifax, B3H 3C3, Canada; vorobyov@ap.smu.ca.

² Research Institute of Physics, South Federal University, Stachki 194, Rostov-on-Don, 344090, Russia.

action of the star/disk system with the natal cloud core is of considerable importance for the disk physics and this inevitably requires solving for a much larger spatial volume than in isolated systems. As a consequence, most information about the early evolution of embedded protostellar disks was drawn from one-dimensional numerical studies of thin axisymmetric disks with some approximate prescription for disk gravity and, in some cases, with a solution for the vertical disk structure in the so-called 1+1D approximation (e.g. Lin & Pringle 1990; Bell & Lin 1994; Nakamoto & Nakagawa 1994; Hueso & Guillot 2005; Visser et al. 2009; Rice et al. 2010). Alternatively, analytic models of protostellar disks subject to intense mass loading have been constructed, which cover a wide parameter space and can yield important information than can later be compared against more focused numerical hydrodynamics simulations (e.g. Kratter et al. 2008; Clarke 2009; Krumholz & Burkert 2010).

Some interesting insight into the early disk evolution, accretion history, and velocity structure of the infalling gas was also obtained in two-dimensional numerical simulations of axisymmetric disks (e.g. Yorke & Bodenheimer 1999; Boss & Hartmann 2001; Zhu et al. 2009). Unfortunately, such simulations cannot describe self-consistently mass and angular momentum transport due to gravitational torques, which cannot develop in axisymmetric disks. To resolve this problem, some sort of effective viscosity is often invoked. An alternative two-dimensional approach involves solving for the evolution of protostellar disks in the thin-disk approximation, which allows for an accurate treatment of gravitational torques (e.g. Nelson et al. 2000; Johnson & Gammie 2003). These studies revealed the importance of disk cooling for the development of gravitational instability and fragmentation but suffered from the lack of disk interaction with a natal cloud core in the EPSF.

An important step forward was done in a series of papers by Vorobyov & Basu (2005, 2006, 2009a,b) and Vorobyov (2009a,b, 2010) who employed two-dimensional numerical simulations in the thin-disk approximation with an accurate treatment of disk self-gravity to model self-consistently the formation and evolution of protostellar disks. These studies have demonstrated that mass loading onto the disk from the infalling envelope can bring about qualitatively new phenomena such as the burst mode of accretion (Vorobyov & Basu 2005, 2006, 2010b) and formation of giant planets on wide orbits (Vorobyov & Basu 2010a). Such two-dimensional simulations allow us to consider the long-term evolution of a large number of self-consistently formed protostellar disks at the expense of the detailed disk vertical structure.

First fully three-dimensional simulations, though suffering from insufficient numerical resolution, have revealed important information about the vertical structure of the disks and their susceptibility to gravitational instability and fragmentation (e.g. Laughlin & Bodenheimer 1994; Burkert et al. 1997; Boss 1998; Pickett et al. 2000). With the advent of more powerful computers and techniques, new and more detailed three-dimensional numerical simulations of the formation and evolution of protostellar disks have started to emerge (Krumholz et al. 2007; Boley 2009; Boley et al.

2009; Kratter et al. 2010a; Machida et al. 2010). Unfortunately, due to still enormous computational load involved, these studies often suffer from restricted parameter space, limited temporal and spatial resolution, simplified treatment of the gas infall onto the disk, and/or the lack of detailed thermal physics. In addition, due to severe resolution limitations, 3D numerical simulations often resort to the use of sink particles to trace forming stellar and planetary objects, which inevitably involves introducing additional free parameters into the model.

This is the second paper in a series addressing the physical properties of *embedded* protostellar disks. In the first paper (Vorobyov & Basu 2010b), we have mainly focused on the burst mode of accretion that develops in fragmenting disks. In this paper, we perform a comprehensive numerical hydrodynamics study of the formation and long-term evolution of protostellar disks formed from cloud cores of distinct mass and rotational energy. We make use of the thin-disk approximation complemented by a detailed calculation of the disk thermal balance. Several models were scrutinized to derive the detailed disk structure and time evolution. Our numerical studies can serve as a framework for the future high-resolution observations of embedded disks using such ground-based or space-based facilities as ALMA or Millimetron (Wild et al. 2009). The paper is organized as follows. In § 2, we review our numerical model and initial setup. The structure and evolution of protostellar disks formed from cloud cores of distinct mass and rotational energy are presented in § 3 and § 4. The main conclusions are summarized in § 5.

2. MODEL DESCRIPTION

The main concepts of our numerical approach are explained in detail in Vorobyov & Basu (2010b) and, for the reader's convenience, are briefly reviewed below. We start our numerical integration in the pre-stellar phase, which is characterized by a collapsing *starless* cloud core, continue into the embedded phase of star formation, during which a star, disk, and envelope are formed, and terminate our simulations in the T Tauri phase, when most of the envelope has accreted onto the forming star/disk system. In the EPSF, the disk occupies the innermost region of our numerical grid, while the larger outer part of the grid is taken up by the infalling envelope, the latter being the remnant of the parent cloud core. This ensures that the protostellar disk is not isolated in the EPSF but is exposed to intense mass loading from the envelope. In addition, the mass accretion rate onto the disk \dot{M}_{env} is not a free parameter of the model but is self-consistently determined by the gas dynamics in the envelope.

We introduce a “sink cell” at $r_{\text{sc}} = 6$ AU and impose a free inflow inner boundary condition and free outflow outer boundary condition so that that the matter is allowed to flow out of the computational domain but is prevented from flowing in. We monitor the gas surface density in the sink cell and when its value exceeds a critical value for the transition from isothermal to adiabatic evolution, we introduce a central point-mass star. In the subsequent evolution, 90% of the gas that crosses the inner boundary is assumed to land onto the central star plus the inner axisymmetric disk at $r < 6$ AU. This inner disk is dynamically inactive; it contributes only to the total gravitational potential and is used to secure a

smooth behaviour of the gravity force down to the stellar surface. The other 10% of the accreted gas is assumed to be carried away with protostellar jets. The latter are triggered only after the formation of the central star.

2.1. Basic equations

We make use of the thin-disk approximation to compute the gravitational collapse of rotating, gravitationally unstable cloud cores. This approximation is an excellent means to calculate the evolution for many orbital periods and many model parameters. The basic equations of mass, momentum, and energy transport are

$$\frac{\partial \Sigma}{\partial t} = -\nabla_p \cdot (\Sigma \mathbf{v}_p), \quad (1)$$

$$\frac{\partial}{\partial t} (\Sigma \mathbf{v}_p) + [\nabla \cdot (\Sigma \mathbf{v}_p \otimes \mathbf{v}_p)]_p = -\nabla_p \mathcal{P} + \Sigma \mathbf{g}_p + (\nabla \cdot \mathbf{\Pi})_p, \quad (2)$$

$$\frac{\partial e}{\partial t} + \nabla_p \cdot (e \mathbf{v}_p) = -\mathcal{P}(\nabla_p \cdot \mathbf{v}_p) - \Lambda + \Gamma + (\nabla \mathbf{v})_{pp'} : \mathbf{\Pi}_{pp'}, \quad (3)$$

where subscripts p and p' refers to the planar components (r, ϕ) in polar coordinates, Σ is the mass surface density, e is the internal energy per surface area, $\mathcal{P} = \int_{-Z}^Z P dz$ is the vertically integrated form of the gas pressure P , Z is the radially and azimuthally varying vertical scale height determined in each computational cell using an assumption of local hydrostatic equilibrium, $\mathbf{v}_p = v_r \hat{\mathbf{r}} + v_\phi \hat{\boldsymbol{\phi}}$ is the velocity in the disk plane, $\mathbf{g}_p = g_r \hat{\mathbf{r}} + g_\phi \hat{\boldsymbol{\phi}}$ is the gravitational acceleration in the disk plane, and $\nabla_p = \hat{\mathbf{r}} \partial / \partial r + \hat{\boldsymbol{\phi}} r^{-1} \partial / \partial \phi$ is the gradient along the planar coordinates of the disk.

Viscosity enters the basic equations via the viscous stress tensor $\mathbf{\Pi}$ expressed as

$$\mathbf{\Pi} = 2\Sigma\nu \left(\nabla \mathbf{v} - \frac{1}{3}(\nabla \cdot \mathbf{v}) \mathbf{e} \right), \quad (4)$$

where \mathbf{e} is the unit tensor. We note that we take no simplifying assumptions about the form of $\mathbf{\Pi}$ apart from those imposed by the adopted thin-disk approximation. We parameterize the magnitude of kinematic viscosity ν using a modified form of the α -prescription

$$\nu = \alpha c_s Z \mathcal{F}_\alpha(r), \quad (5)$$

where $c_s^2 = \gamma \mathcal{P} / \Sigma$ is the square of effective sound speed calculated at each time step from the model's known \mathcal{P} and Σ . The function $\mathcal{F}_\alpha(r) = 2\pi^{-1} \tan^{-1} [(r_d/r)^{10}]$ is a modification to the usual α -prescription that guarantees that the turbulent viscosity operates only in the disk and quickly reduces to zero beyond the disk radius r_d . In this paper, we use a spatially and temporally uniform α , with its value set to 5×10^{-3} based on our recent work (Vorobyov & Basu 2009b). Our adopted value of α are in agreement with the mean value inferred by Andrews et al. (2009) for a large sample of protostellar disks in the Ophiuchus star-forming region.

Equation (3) for the internal energy (per surface area) transport includes compressional heating $\mathcal{P}(\nabla_p \cdot \mathbf{v}_p)$, radiative cooling Λ , heating due to stellar/background irradiation Γ , and viscous heating $(\nabla \mathbf{v})_{pp'} : \mathbf{\Pi}_{pp'}$. The

cooling function is determined using the diffusion approximation of the vertical radiation transport in a one-zone model of the vertical disk structure (Johnson & Gammie 2003)

$$\Lambda = \mathcal{F}_c \sigma T^4 \frac{\tau}{1 + \tau^2}, \quad (6)$$

where σ is the Stefan-Boltzmann constant, T is the mid-plane temperature of gas, and $\mathcal{F}_c = 2 + 20 \tan^{-1}(\tau) / (3\pi)$ is a function that secures a correct transition between the cooling function (from both surfaces of the disk) in the optically thick regime $\Lambda_{\text{thick}} = 16 \sigma T^4 / 3\tau$ and the optically thin one $\Lambda_{\text{thin}} = 2 \sigma T^4 \tau$. We use frequency-integrated opacities of Bell & Lin (1994)

The heating function is expressed as

$$\Gamma = \mathcal{F}_c \sigma T_{\text{irr}}^4 \frac{\tau}{1 + \tau^2}, \quad (7)$$

where T_{irr} is the irradiation temperature at the disk surface determined by the stellar and background black-body irradiation as

$$T_{\text{irr}}^4 = T_{\text{bg}}^4 + \frac{F_{\text{irr}}(r)}{\sigma}, \quad (8)$$

where T_{bg} is the uniform background temperature (in our model set to the initial temperature of the natal cloud core) and $F_{\text{irr}}(r)$ is the radiation flux (energy per unit time per unit surface area) absorbed by the disk surface at radial distance r from the central star. The latter quantity is calculated as

$$F_{\text{irr}}(r) = A_{\text{irr}} \frac{L_*}{4\pi r^2} \cos \gamma_{\text{irr}}, \quad (9)$$

where γ_{irr} is the incidence angle of radiation arriving at the disk surface at radial distance r and $A_{\text{irr}} = M_{\text{cl}} / (M_{\text{env}} + M_{\text{cl}})$ is a time-dependent factor that accounts for the attenuation of stellar radiation by the envelope with mass M_{env} in three-dimensional disks and takes values from $\gtrsim 0.5$ at the disk formation to ≈ 1.0 at the end of the EPSF and beyond³. The stellar luminosity L_* is the sum of the accretion luminosity $L_{*,\text{accr}} = GM_* \dot{M} / 2r_*$ arising from the gravitational energy of accreted gas and the photospheric luminosity $L_{*,\text{ph}}$ due to gravitational compression and deuterium burning in the star interior. The stellar mass M_* and accretion rate onto the star \dot{M} are determined self-consistently during numerical simulations via the amount of gas passing through the sink cell. The stellar radius r_* is calculated using an approximation formula of Palla & Stahler (1991), modified to take into account the formation of the first molecular core (Masunaga & Inutsuka 2000). The photospheric luminosity $L_{*,\text{ph}}$ is taken from the pre-main sequence tracks for the low-mass stars and brown dwarfs calculated by D'Antona & Mazitelli (1997). More details are given in Vorobyov & Basu (2010b).

Viscous heating operates in the disk interior and is calculated using the standard expression $(\nabla \mathbf{v})_{pp'} : \mathbf{\Pi}_{pp'}$.

³ Although most of the envelope material should be landing onto the disk outer edge, a smaller fraction may still be falling onto the disk inner regions (Visser et al. 2009) and this material may intercept some of the stellar radiation in the EPSF. The effect of this attenuation factor on the disk evolution is however not significant, since its value quickly approaches unity. For instance in model 3, $A_{\text{irr}} \approx 0.75$ at $t = 0.1$ Myr after the disk formation and $A_{\text{irr}} \approx 0.95$ at $t = 0.3$ Myr.

TABLE 1
MODEL CLOUD CORE PARAMETERS

Model	M_{cl}	β	Ω_0	r_0	Σ_0
1	0.2	5.6×10^{-3}	6.2	445	0.28
2	0.85	5.6×10^{-3}	1.5	1885	0.066
3	1.7	5.6×10^{-3}	0.7	3770	0.033
4	0.85	2.8×10^{-3}	1.0	1885	0.066
5	0.85	2.3×10^{-2}	2.9	1885	0.066

NOTE. — All masses are in M_\odot , distances in AU, surface densities in g cm^{-2} , and angular velocities in $\text{km s}^{-1} \text{pc}^{-1}$.

Heating due to shock waves is taken into account via compressional heating $\mathcal{P}(\nabla_p \cdot \mathbf{v}_p)$ and artificial viscosity, the latter implemented in the code using the standard prescription of Richtmyer & Morton (1957). The vertically integrated gas pressure \mathcal{P} and internal energy per surface area e are related via the ideal equation of state $\mathcal{P} = (\gamma - 1)e$, with the ratio of specific heats $\gamma = 7/5$.

Equations (1)–(3) are solved using the method of finite differences with a time explicit solution procedure in polar coordinates (r, ϕ) on a numerical grid with 512×512 grid zones. The advection is treated using the van Leer interpolation scheme. The update of the internal energy per surface area e due to cooling Λ and heating Γ is done implicitly using the Newton-Raphson method of root finding, complemented by the bisection method where the Newton-Raphson iterations fail to converge. The viscous heating and force terms in Equations (2) and (3) are implemented in the code using an explicit finite-difference scheme, which is found to be adequate for $\alpha \lesssim 0.01$. The radial points are logarithmically spaced. The innermost grid point is located at the position of the sink cell $r_{\text{sc}} = 6$ AU, and the size of the first adjacent cell varies in the 0.07–0.1 AU range depending on the cloud core size. This corresponds to the radial resolution of $\Delta r = 1.1$ –1.6 AU at 100 AU.

2.2. Initial conditions

Initially isothermal ($T_{\text{init}} \equiv T_{\text{bg}} = 10$ K) cloud cores have surface densities Σ and angular velocities Ω typical for a collapsing, axisymmetric, magnetically supercritical core (Basu 1997)

$$\Sigma = \frac{r_0 \Sigma_0}{\sqrt{r^2 + r_0^2}}, \quad (10)$$

$$\Omega = 2\Omega_0 \left(\frac{r_0}{r}\right)^2 \left[\sqrt{1 + \left(\frac{r}{r_0}\right)^2} - 1 \right], \quad (11)$$

where Ω_0 is the central angular velocity and r_0 is the radius of central near-constant-density plateau defined as $r_0 = \sqrt{A c_s^2 / (\pi G \Sigma_0)}$, with the initial positive density enhancement A set to 1.2 throughout the paper. Model cores are characterized by a distinct ratio $r_{\text{out}}/r_0 = 6$ in order to generate gravitationally unstable truncated cores of similar form, where r_{out} is the cloud core's outer radius.

For the in-depth analysis of circumstellar disk structure and evolution, we have chosen five typical model cloud cores with varying initial cloud core masses M_{cl} and ratios $\beta = E_{\text{rot}}/|E_{\text{grav}}|$ of the rotational to gravita-

tional energy defined as

$$E_{\text{rot}} = 2\pi \int_{r_{\text{sc}}}^{r_{\text{out}}} r a_c \Sigma r dr, \quad (12)$$

$$E_{\text{grav}} = -2\pi \int_{r_{\text{sc}}}^{r_{\text{out}}} r g_r \Sigma r dr, \quad (13)$$

respectively, where $a_c = \Omega^2 r$ is the centrifugal acceleration. The parameters of these models are listed in Table 1. We note that cloud cores with the adopted values of M_{cl} are expected to form solar- and sub-solar type stars and the values of β lie within the limits inferred by Caselli et al. (2002) for dense molecular cloud cores, $\beta = (10^{-4} - 0.07)$.

In the following text, we consider separately models with distinct M_{cl} but similar β (models 1, 2, and 3) and distinct β but similar M_{cl} (models 2, 4, and 5). In particular, the parameter β is varied by changing the value of Ω_0 only. These two sets of models have been chosen to single out the effects of increasing cloud core masses, from one hand, and increasing rotational energies of cloud cores, from the other hand. We note that the original cloud core mass and rotation rate are expected to have a major impact on the evolution of a protostellar disk because they determine the centrifugal radius and, consequently, the disk mass and stability properties.

3. DISK STRUCTURE AND EVOLUTION ALONG THE LINE OF INCREASING CLOUD CORE MASSES

We start by considering the properties of protostellar disks formed from cloud cores of increasingly higher mass M_{cl} . In particular, model 1 is characterized by $M_{\text{cl}} = 0.2 M_\odot$, while models 2 and 3 have $M_{\text{cl}} = 0.85 M_\odot$ and $M_{\text{cl}} = 1.7 M_\odot$, respectively. The ratio β is identical for these models and is set to 5.6×10^{-3} .

3.1. Face-on disk images

Figure 1 presents gas surface densities (in g cm^{-2} , log units) in model 1 (top row), model 2 (middle row) and model 3 (bottom row) at four distinct times after the disk formation (from left to right): $t=0.1$ Myr, $t=0.3$ Myr, $t=0.5$ Myr, and $t=0.7$ Myr. We note that the spatial scale is different for model 1 (400×400 AU), model 2 (800×800 AU), and model 3 (1100×1100 AU). Superimposed on the gas surface density images are the gas velocity fields (arrows) and yellow contour lines. The latter delineate disk regions that are characterized by the frequency-averaged optical depth $\tau \geq 0.1$. Optical depth effects are expected to become important in these regions.

It is evident that the disk appearance in Figure 1 changes significantly along both the line of increasing cloud core mass (from top to bottom) and the line of growing disk age (from left to right). The disk in the $M_{\text{cl}} = 0.2 M_\odot$ model 1 (top row) demonstrates a weak, diffuse spiral structure at $t = 0.1$ Myr and becomes nearly perfectly axisymmetric in the subsequent evolution. On the other hand, the disk in the $M_{\text{cl}} = 0.85 M_\odot$ model 2 (middle row) exhibits a rich, well-defined spiral structure at $t = 0.1$ Myr, which weakens and diffuses with time but still can be traced in the 0.5-Myr-old disk.

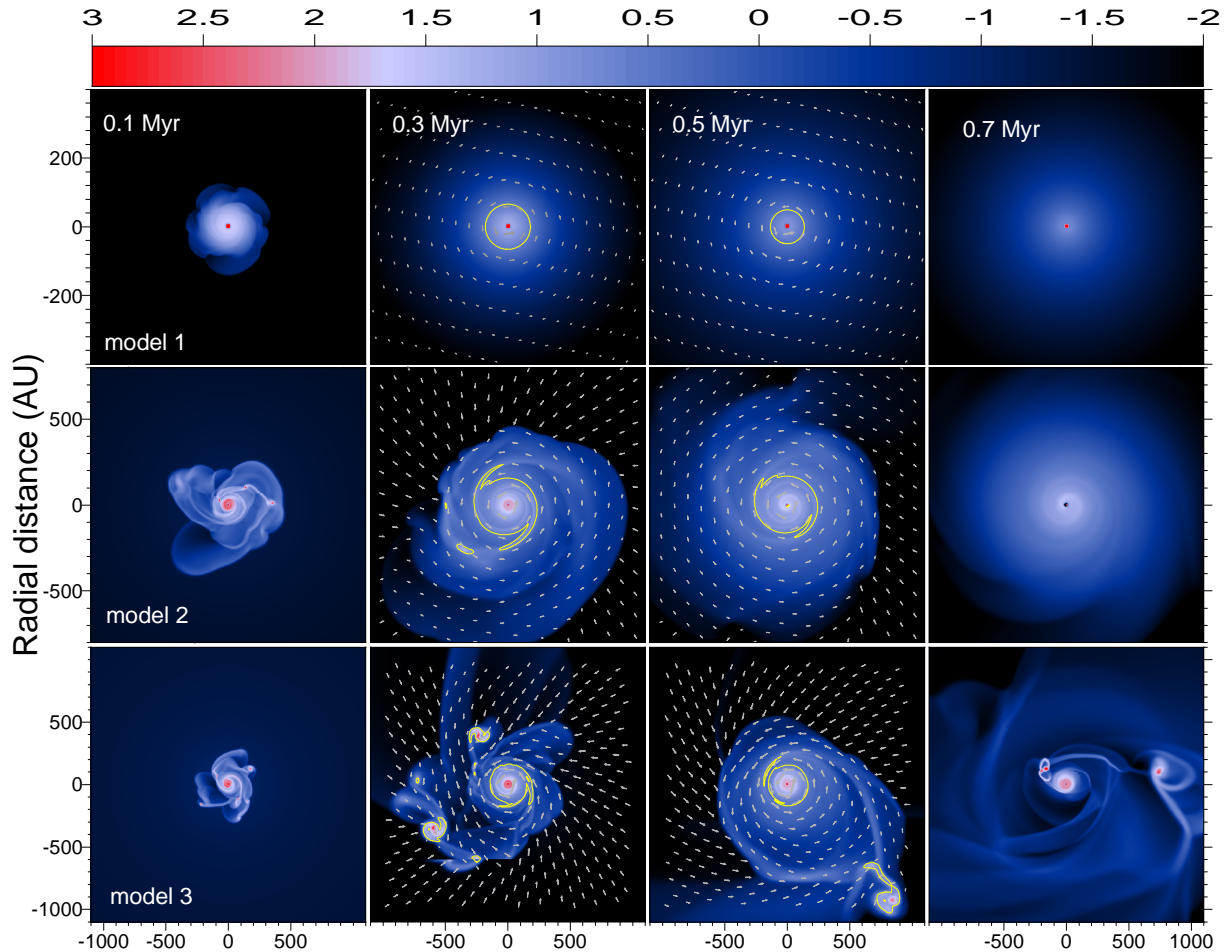


FIG. 1.— Gas surface density (in g cm^{-2} , log units) in three models with distinct cloud core mass M_{cl} and at distinct times t after the disk formation. In particular, the top row shows disk images in the $M_{\text{cl}} = 0.2 M_{\odot}$ model, while the middle and bottom rows present those of the $M_{\text{cl}} = 0.85 M_{\odot}$ and $M_{\text{cl}} = 1.7 M_{\odot}$ models, respectively. Columns from left to right correspond to $t = 0.1$ Myr, $t = 0.3$ Myr, $t = 0.5$ Myr, and $t = 0.7$ Myr, respectively. Superimposed on the disk images are the gas velocity fields (arrows) and yellow contour lines delineating disk regions with the frequency-integrated optical depth $\tau \geq 0.1$.

Fragmentation of the spiral arms (small red clumps in the middle-left panel) occurs at $t=0.1$ Myr after the disk formation. However, no survived fragments are seen at later times due to an efficient migration mechanism⁴ that operates in the EPSF and drives the fragments into the inner disk regions and through the sink cell, causing accretion and luminosity bursts (Vorobyov & Basu 2005, 2006, 2010b). An apparent lopsidedness is evident in the 0.3-Myr-old and 0.5-Myr-old disks but seems to diminish at later times. The gas velocity field indicates considerable non-circular motions within the disk, suggesting the existence of local deviations from a Keplerian rotation. In addition, notable non-axisymmetric variations in the disk shape suggest that an axisymmetric description of a circumstellar disk in the early evolution stage is unjustified, at least on time scales of the order of 0.5 Myr after the disk formation.

The $M_{\text{cl}} = 1.7$ model 3 (bottom row in Figure 1) is most extreme and demonstrates vigorous gravitational instability and fragmentation. Two well-defined fragments possessing counterrotating minidisks and a few smaller ones are seen in the 0.3-Myr-old disk (note that

the disk rotates counterclockwise). The counterrotation can clearly be seen in Figure 2, which shows the residual velocity field superimposed on the gas surface density in model 3 at $t = 0.3$ Myr. The residuals are obtained by subtracting the Keplerian rotation from the total gas velocity, thus accentuating the gas motion in a local frame of reference moving with the disk. Considerable non-Keplerian motions are also evident near/at the spiral arms.

Such counterrotating structures may owe their existence to differential rotation of fragmenting spiral arms. When a fragment forms near corotation⁵, it captures gravitationally some of the neighboring material, which receives a counterrotating twist around the forming fragment due to the fact that the inner parts of the arm rotate around the central star faster than the outer ones. It is important to note that this mechanism is not universal and, as found in other runs (Vorobyov & Basu 2010b), some fragments may also possess corotating minidisks. It is feasible that the direction of rotation is determined by local conditions at the position of the forming fragment (e.g. spiral arm structure and density, residual velocity field, etc.), in which case it is difficult to predict the

⁴ See animation of this quick migration at www.astro.uwo.ca/~vorobyov (animations: burst mode of accretion).

⁵ Fragmentation of spiral arms occurs preferentially near corotation where distortion due to differential rotation is minimal.

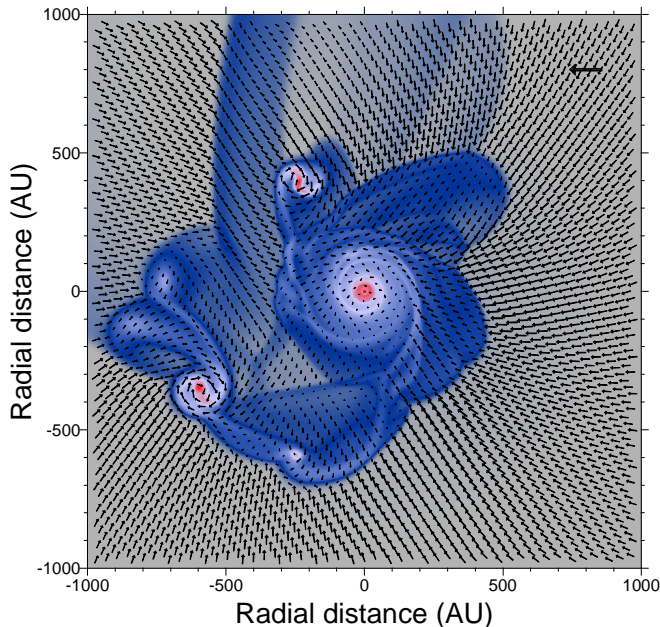


FIG. 2.— Residual velocity field (total velocity field minus Keplerian rotation) superimposed on the gas surface density in model 3 at $t=0.3$ Myr after the disk formation. The horizontal arrow in the right-upper corner has a dimension of 5 km s^{-1} . In the simulation, the disk rotates counterclockwise and two fragments with disk rotating clockwise are clearly visible.

outcome. We plan to study this phenomenon in greater detail in a future paper.

In the 0.5-Myr-old disk, most of the fragments have either been destroyed or absorbed by the central star. However, one fragment has survived and a binary system with the smaller companion possessing a sizeable counterrotating disk has emerged. The separation between the companions is about 1000 AU and the masses of the primary/secondary are approximately $M_* = 0.95 M_\odot$ and $M_{\text{sec}} = 0.15 M_\odot$, respectively, with the latter value being an upper limit on both the companion and its minidisk. The fragmentation process continues even in the 0.7-Myr-old system and another fragment with mass $\leq 0.08 M_\odot$ emerges in the disk of the primary at $r \approx 200$ AU. In the meantime, the outer fragment has migrated inward to approximately 720 AU. The subsequent evolution of the system is uncertain since we terminate the simulation due to enormous computational load. We hope that model 3 can ultimately evolve into a binary or triple system with low-mass ratio and (at least) one of the companion being in the brown dwarf mass regime.

Three interesting features in Figure 1 are worth of specific emphasis. First, young protostellar disks ($t \lesssim 0.1$ Myr) are conspicuously non-axisymmetric, even in the $M_{\text{cl}} = 0.2 M_\odot$ model, but evolve with time toward a more regular, axisymmetric state. However, the rate of this evolution is much faster in models with lower cloud core masses. This is primarily caused by the fact that mass loading from the infalling envelope is the main driving force that sustains gravitational instability in the disk and the duration of this infall (i.e., the lifetime of the EPSF) is near-linearly proportional to the cloud core mass (Vorobyov 2010). Second, a fairly large portion of the disk, irrespective of the model, is characterized by $\tau > 0.1$, which implies that the optical depth effect cannot be neglected in the early evolution of protostellar

disks. We will return to this question in more detail in § 3.2. Finally, sufficiently massive cloud cores may form binary or multiple systems with brown dwarf and/or sub-solar companions. In the future higher-resolution simulations, we hope to see planetary-mass objects forming in the disk.

3.2. Disk radial structure

Due to limited spatial resolution of modern observational facilities at long wavelengths, vital information about the structure of protostellar disks is often retrieved from modeling the spectral energy distribution based on analytical disk models that assume gas surface densities and temperatures to be power laws in radius (e.g. Looney et al. 2003; Andrews & Williams 2005; Andrews et al. 2009). Our numerical simulations can provide a useful starting point for such an analysis by constructing the typical azimuthally-averaged radial profiles of various physical characteristics of protostellar disks.

Figure 3 presents such radial profiles for the gas surface density $\bar{\Sigma}$ (first row), midplane gas temperature \bar{T} (second row), optical depth $\bar{\tau}$ (third row), enclosed mass $M(r)$ (forth row), and angular velocity $\bar{\Omega}$ (fifth row). In particular, black solid lines correspond to model 1, while black dashed and dash-dotted lines present the data for models 2 and 3, respectively. The vertical columns from left to right correspond to four distinct times after the disk formation: $t = 0.1$ Myr, $t = 0.3$ Myr, $t = 0.5$ Myr, and $t = 0.7$ Myr. The vertical dotted lines show the disk radii r_d in model 1 (left line) and model 2 (right line) as derived from a characteristic gas surface density of $\Sigma_{\text{d2e}} = 0.1 \text{ g cm}^{-2}$ for the disk to envelope transition and radial gas velocity (see Vorobyov 2010, for details). The horizontal dotted lines in the third row mark characteristic optical depths of $\bar{\tau}=1$ (top) and $\bar{\tau}=0.1$ (bottom). The sloped dotted lines in the bottom row show the angular velocity of a pressure-free gas in the gravitational field of a $5.0 M_\odot$ star. The red solid and dashed lines and also the blue dashed line are the best fits to the model gas density and temperature distributions.

The top row in Figure 3 demonstrates that protostellar disks of *equal* age formed from cloud cores of greater mass are generally characterized by higher gas surface densities $\bar{\Sigma}$, larger radii r_d , and, consequently, greater masses M_d . For instance, the 0.1-Myr-old disk in model 1 has $\bar{\Sigma}(r = 20 \text{ AU}) = 42 \text{ g cm}^{-2}$, $r_d = 117 \text{ AU}$, and $M_d = 0.03 M_\odot$, while the corresponding values in model 2 are $\bar{\Sigma}(r = 20 \text{ AU}) = 208 \text{ g cm}^{-2}$, $r_d = 378 \text{ AU}$, and $M_d = 0.2 M_\odot$. This tendency is a mere consequence of an increased mass reservoir in the envelope, increased mass infall rate onto the disk, and insufficiently fast radial mass transport in low-mass disks dominated by viscous torques with typical α of the order of 0.005–0.01. As a result, low-mass disks cannot efficiently transport matter from the disk’s outer edge (where most of the envelope gas lands) onto the forming star and the disk starts to grow both in mass and radius. A similar tendency of T Tauri disks being in general denser and hotter than those of substellar objects was also found by Wiebe et al. (2008).

However, the trend of more massive cloud cores to form denser disks becomes much less pronounced for cores with $M_{\text{cl}} \gtrsim 0.9 M_\odot$. Indeed, the azimuthally-

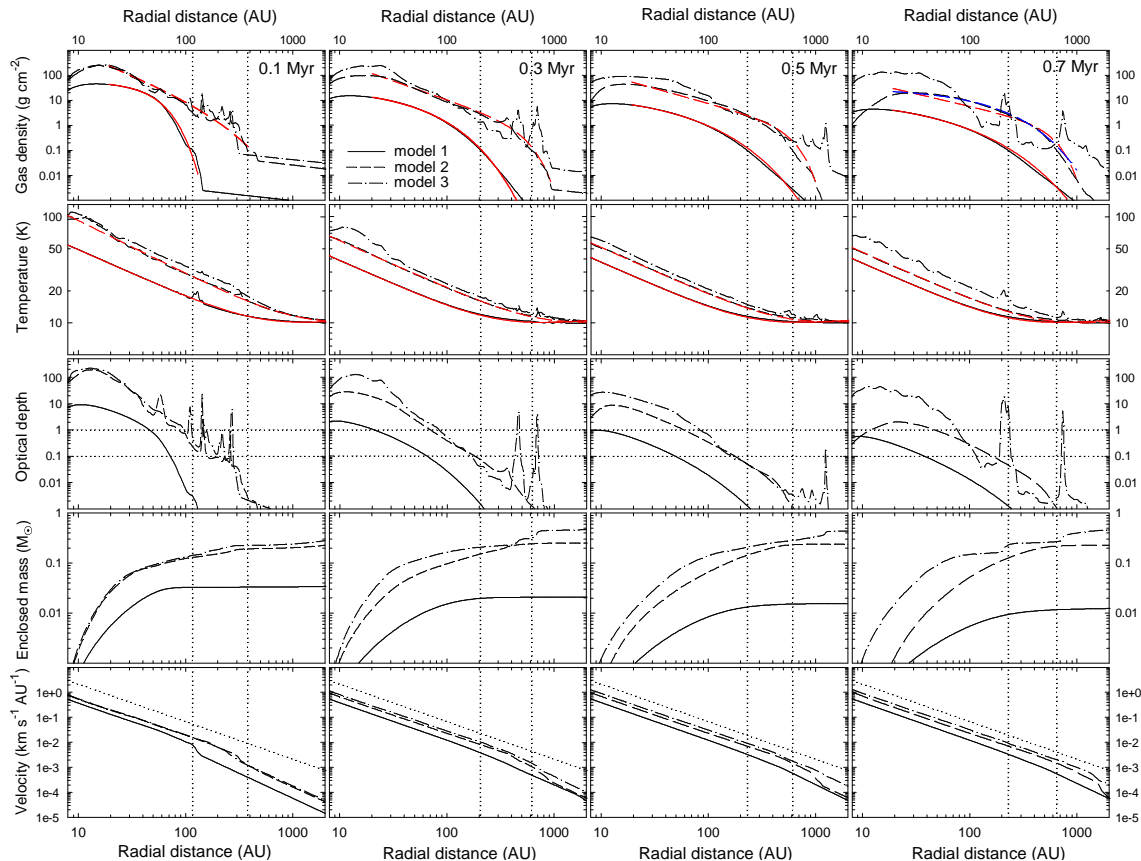


FIG. 3.— Azimuthally-averaged radial profiles of the gas surface density $\bar{\Sigma}$ (first row), gas midplane temperature \bar{T} (second row), frequency-integrated optical depth $\bar{\tau}$ (third row), and angular velocity $\bar{\Omega}$ (fifth row). The fourth row presents the enclosed mass $M(r)$ as a function of radius. The vertical columns from left to right show the data at different times after the disk formation: $t=0.1$ Myr, $t=0.3$ Myr, $t=0.5$ Myr, and $t=0.7$ Myr. The solid, dashed, and dash-dotted lines present the data for the $M_{\text{cl}} = 0.2 M_{\odot}$ model 1, $M_{\text{cl}} = 0.85 M_{\odot}$ model 2, and $M_{\text{cl}} = 1.7 M_{\odot}$ model 3, respectively. The red solid and dashed lines are the best fits to the model gas surface density and midplane temperature distributions in model 1 and model 2, respectively. The vertical dotted lines mark the position of the disk outer edge in model 1 (left lines) and model 2 (right lines). The horizontal dotted lines are the characteristic optical depths of $\tau = 1.0$ and $\tau = 0.1$. The sloped dotted lines in the bottom row show the angular velocity of a pressure-free gas in the gravitational field of a $5.0 M_{\odot}$ star.

averaged gas surface density in model 3 is only marginally higher than in model 2, indicating the onset of a self-regulatory state in which the disk grows in size and mass (due to continuing mass loading from the infalling envelope) rather than in gas surface density. This effect is caused by vigorous gravitational instability and fragmentation that develop in the EPSF. Indeed, as Figure 1 demonstrates, the $M_{\text{cl}} = 0.2 M_{\odot}$ model 1 reveals a rather weak spiral structure, while the protostellar disk in the $M_{\text{cl}} = 1.7 M_{\odot}$ model 3 is conspicuously non-axisymmetric, showing a well-defined spiral structure and multiple fragments forming in the arms. These fragments migrate radially inward and onto the star during a few tens of orbital periods (often on even shorter timescales), thus effectively restricting the growth of the disk surface density and bringing the disk back to the border of stability after every fragmentation episode.

The behaviour of both the midplane gas temperature (second row in Figure 3) and optical depth (third row) in disks of equal age is similar to that of the gas surface density (top row)—both \bar{T} and $\bar{\tau}$ increase along the sequence of increasing cloud core masses. As in the case with $\bar{\Sigma}$, this trend appears to slow down for models with $M_{\text{cl}} \gtrsim 0.9 M_{\odot}$.

From the third row in Figure 3 it is seen that the inner disk regions and most fragments are optically thick

with $\bar{\tau} > 1.0$, while the outer disk regions are either marginally optically thin ($0.1 < \bar{\tau} < 1.0$) or completely optically thin ($\bar{\tau} < 0.1$). The fact that a substantial fraction of protostellar disks is optically thick may have important consequences for the disk mass estimates using conventional observational techniques. Indeed, the fourth row in Figure 3 presents the enclosed mass $M(r)$ (both that of the disk and the envelope) as a function of radius. It is evident that a considerable fraction of the total mass may be concentrated in regions with $\bar{\tau} > 0.1$, which are expected to be affected by a non-negligible optical depth. This is particularly true for the early disk evolution. For instance, the 0.3-Myr-old disk in model 2 has radius $r_{\text{d}} \approx 615$ AU and mass $M_{\text{d}} = 0.24 M_{\odot}$. On the other hand, if we count only those regions that are characterized by $\bar{\tau} > 0.1$ and $\bar{\tau} > 1$, the corresponding disk masses are $0.075 M_{\odot}$ and $0.14 M_{\odot}$, respectively, indicating that as much as 70% of the total mass content may be hidden from our sight. As Figure 3 demonstrates, both $\bar{\Sigma}$ and $\bar{\tau}$ express a tendency to decrease with time, implying that the observationally inferred disk mass are expected to be more accurate for disks of older age.

The bottom row in Figure 3 reveals that the azimuthally-averaged angular velocity has a near-Keplerian profile, notwithstanding conspicuous local deviations from a circular gas motion evident in Figure 1.

In addition, the outer disk regions exhibit a slightly over-Keplerian rotation, most likely due to an additive effect from the gravitational field of the inner disk regions.

It is useful to construct some functions that approximate and summarize our model radial profiles of $\bar{\Sigma}$ and \bar{T} for disks of distinct age. To fit our model data, we use the following two functions

$$\bar{\Sigma} = \Sigma_0 \left(\frac{1 \text{ AU}}{r} \right)^{n_1} \exp \left[- \left(\frac{r}{a} \right)^m \right], \quad (14)$$

$$\bar{T} = T_0 \left(\frac{1 \text{ AU}}{r} \right)^{n_2} + T_{\text{bg}} \left(\frac{r}{r+b} \right), \quad (15)$$

where r is the radial distance in AU, T_0 and Σ_0 are the gas temperature (in Kelvin) and gas surface density (in g cm^{-2}) at 1 AU, respectively⁶. The form of Equation (14) is chosen to approximate $\bar{\Sigma}$ in the disk inner and intermediate regions by a power-law function, while the disk outer regions, which are usually characterized by gas surface density falling off with radius faster than a power-law, are approximated by an exponential function. However, if n_1 is set to zero, Equation (14) approximates the whole disk by a sole exponential function. In the case of $n_1 \neq 0$, the parameters m and a express the steepness of $\bar{\Sigma}$ near the disk outer edge and the approximate radial position of the disk outer edge, respectively. In the case of $n_1 = 0$, the aforementioned parameters express the steepness and the characteristic radius of the radial gas surface density distribution in the whole disk. The form of Equation (15) is motivated by the fact that the radial gas temperature distribution in the midplane of a flared disk is usually well approximated by a power-law function, while the right-hand-side term in Equation (15) is invoked to make a smooth transition between the disk and the envelope, the latter being characterized by a background temperature T_{bg} . The parameter b represents the radial position beyond which the gas thermal balance is controlled by the external background radiation with temperature T_{bg} rather than by stellar irradiation or viscous heating.

Red lines in the upper two rows of Figure 3 present our best fits to the model radial distributions of $\bar{\Sigma}$ and \bar{T} . More specifically, the red solid and dashed lines are the best fits to model 1 and 2, respectively. We do not fit model 3, since its radial profiles are not significantly dissimilar to those of model 2. To fit the model data, we use the Marquardt-Lovénberg algorithm. Because the fitting functions (14) and (15) have too many free parameters, this iterative algorithm takes to many iterations and often does not converge to reliable fits. Therefore, we vary manually the values of n_1 , n_2 , and a until the best agreement with the model data is achieved and obtain the best-fit values for Σ_0 , T_0 , m , and b . In both models, T_{bg} is set to 10 K.

We note that Equation (14) is meant to approximate the gas surface density distribution of the disk only, while Equation (15) does that for the midplane temperature of both the disk and the envelope. In addition, we fit the disk surface density only for $r \geq 20$ AU and exclude the inner disk regions at $r < 20$ AU, where a local peak/flattening in $\bar{\Sigma}$ is often seen. This feature

TABLE 2
BEST FIT PARAMETERS TO RADIAL PROFILES OF $\bar{\Sigma}$ AND \bar{T}

Model	Age	Σ_0	n_1	a	m	T_0	n_2	b
1	0.1	56	0	40	1.8	138	0.45	1475
1	0.3	35	0	22	0.8	110	0.45	900
1	0.5	21	0	14	0.6	105	0.45	820
1	0.7	14	0	13	0.5	103	0.45	790
2	0.1	41150	1.7	150	1.0	290	0.5	3050
2	0.3	10500	1.5	500	2.3	170	0.45	2290
2	0.5	1870	1.2	550	2.5	145	0.45	1615
2	0.7	575	1.0	550	2.5	130	0.45	1370
2	0.7	31	0	80	0.8	130	0.45	1370

NOTE. — Disk age is in Myr, Σ_0 in g cm^{-2} , T_0 in Kelvin, and a and b are in AU.

is hardly present in the corresponding radial profiles of \bar{T} . This local maximum or flattening in $\bar{\Sigma}$ is seen in many multidimensional numerical simulations of circumstellar disks with accretion onto a forming star (e.g. Laughlin & Bodenheimer 1994; Krumholz et al. 2007; Kratter et al. 2010a). In our numerical simulations this feature is likely caused by an absorbing inner computational boundary—the disk material is allowed to freely flow through the sink cell but is not allowed to flow out of it. Indeed, we ran a few models with a smaller sink cell ($r_{\text{sc}}=2$ AU) and found that the position of the peak in $\bar{\Sigma}$ was always located a few AU away from the inner computational boundary.

The resulting best-fit parameters to model radial profiles of $\bar{\Sigma}$ and \bar{T} in models 1 and 2 are listed in Table 2. We find that the radial profiles of $\bar{\Sigma}$ in model 1 are best fitted by a sole exponential function ($n_1 = 0$) rather than by the product of a power-law ($n_1 \neq 0$) and an exponential function. Indeed, the black solid lines in the top panels of Figure 3 show the lack of a distinct slope in the $\log \bar{\Sigma} - \log r$ space. Viscosity-dominated polytropic disks are characterized by radial gas surface density profiles of similar form (Vorobyov & Basu 2009b), suggesting that the disk in model 1 is shaped by viscous torques rather than by gravitational ones. The similarity solution for a viscous disk with $\nu \equiv \alpha c_s Z \propto r^{+1}$ predicts the inverse proportionality of $\bar{\Sigma}$ with radius (Hartmann et al. 1998). The intermediate disk regions are indeed characterized by the “classic” $\bar{\Sigma} \propto r^{-1}$ scaling, which can be expected from the radial temperature dependence $\bar{T} \propto r^{-0.5}$, typical for flared disks, and from the radial vertical scale height dependence $Z \propto r^{1.25}$ obtained in detailed vertical disk structure models of D’Alessio et al. (1999). At the same time, the inner disk regions in model 1 show a shallower than $\bar{\Sigma} \propto r^{-1}$ scaling, while the outer disk regions demonstrate a notably steeper scaling with radius. This steepening may partly be caused by flattening of the corresponding \bar{T} profiles, making the sound speed c_s virtually independent of radius at large radii, and partly by disk flaring, which in our numerical simulations is described by a steeper than D’Alessio et al.’s dependence of Z on radius at large radii (see figure 7 in Vorobyov 2009b).

The radial profiles of $\bar{\Sigma}$ in model 2 (and model 3) show a mixed behaviour. At the early evolution $t \lesssim 0.5$ Myr, they are best fitted by the product of a power-law and exponential function. In the subsequent evolution, how-

⁶ The parameters a and b are usually large numbers.

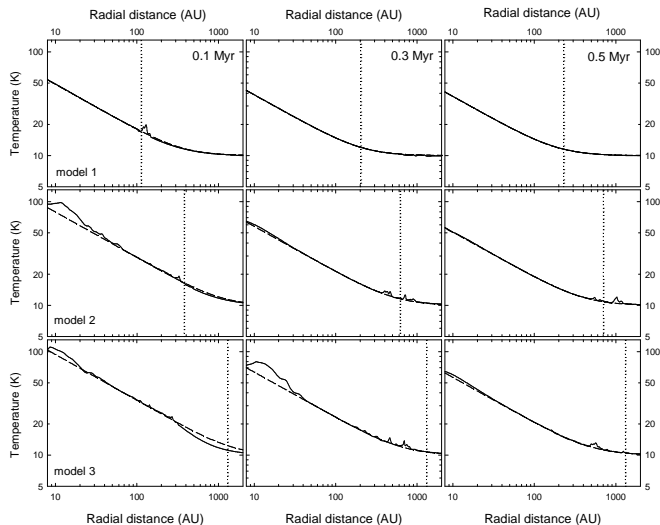


FIG. 4.— Azimuthally-averaged gas midplane temperature \bar{T} (solid lines) and irradiation temperature T_{irr} (dashed lines) as a function of radius in model 1 (top row), model 2 (middle row), and model 3 (bottom row). The left, middle, and right columns are the data obtained at $t = 0.1$ Myr, $t = 0.3$ Myr, and $t = 0.5$ Myr after the disk formation, respectively. The vertical dotted lines mark the position of the disk outer edge in each model.

ever, $\bar{\Sigma}$ begins to approach a pure exponential profile. To demonstrate this trend, we fit the radial profile of $\bar{\Sigma}$ at $t = 0.7$ Myr by both the product of a power-law and an exponential function ($n_1 \neq 0$, red dashed line) and also by a pure exponential function ($n_1 = 0$, blue dashed line). It is obvious that the latter case is more favourable. It is known that protostellar disks dominated by gravity are characterized by gas surface density profiles that scale as $\bar{\Sigma} \propto r^{-1.5}$ (Vorobyov & Basu 2009b; Rice et al. 2010), while the radial profiles of $\bar{\Sigma}$ in viscosity-dominated disks cannot be described by a power-law function with a distinct exponent (Vorobyov & Basu 2009b). This suggests that the 0.5-Myr-old disk in model 2 makes a smooth transition from the gravity-dominated to the viscosity dominated stage.

A visual inspection of Figure 3 reveals that protostellar disks diminish, cool, and expand radially outward with time. This trend is also reflected in the time behaviour of the fitting parameters. For instance, in both models Σ_0 and T_0 decrease with time. Concurrently, the exponents m in model 1 and n_1 in model 2 decline notably with time, indicating a progressive shallowing of the corresponding gas surface density profiles. More specifically, the exponent n_1 takes a value of 1.7 in the 0.1-Myr-old disk of model 2 (early embedded phase) and drops to 1.0 in the 0.7-Myr-old disk (T Tauri phase). In this context, it is interesting to note that T Tauri-type disks in the 1.0-Myr-old Ophiuchus star forming regions reveal $\bar{\Sigma}$ gradients with a mean value of $n_1 \approx 0.9$ (Andrews et al. 2009). The parameter b decreases with time, indicating that the thermal balance in the disk outer regions becomes dominated by the external environment rather than by internal causes such as viscous (or shock) heating or stellar irradiation. We note that while the radial profiles of $\bar{\Sigma}$ shallow with time, the slope of the corresponding radial profiles of \bar{T} , expressed by the exponent n_2 , remains virtually independent of time.

It is interesting to compare the azimuthally-averaged

gas midplane temperature \bar{T} with the irradiation temperature T_{irr} (ϕ -independent) in our model protostellar disks at different stages of the evolution. The difference between the two values determines the extent to which the disk is locally non-isothermal in the vertical direction. Figure 4 presents the radial profiles of \bar{T} (solid lines) and T_{irr} (dashed lines) in model 1 (top row), model 2 (middle row), and model 3 (bottom row). The vertical columns correspond to different disk ages: $t = 0.1$ Myr (left), $t = 0.3$ Myr (middle), and $t = 0.5$ Myr (right). The vertical dotted lines mark the position of the disk outer edge r_d .

It is obvious that the midplane and irradiation temperatures are virtually indistinguishable in the low- M_{cl} model 1, irrespective of the evolutionary stage, indicating that low-mass disks are nearly isothermal in the vertical direction. Only more massive disks formed from cloud cores with $M_{\text{cl}} \gtrsim 0.9 M_{\odot}$ can show a notable negative vertical temperature gradient in the inner disk regions and this phenomenon is localized to the early disk evolution. This temperature gradient is likely caused by viscous heating, which scales as $\Omega^2 \propto r^{-3}$, thus operating preferentially in the disk inner regions (e.g Kratter et al. 2008, 2010a), and also, to a lesser extent, by heating via shock waves with typical for our numerical simulations Mach numbers of the order of 1–2. An example of the latter effect is seen in model 1 near the outer edge of the 0.1-Myr-old disk (upper-left panel), where an accretion shock caused by the infalling envelope creates a local maximum in the gas midplane temperature. We note that in Figure 4 we have averaged the gas midplane temperatures in the azimuthal direction, which may wash out large local azimuthal variations. We find that the gas midplane temperature in dense spiral arms and, especially, in massive fragments can be considerably greater than T_{irr} and reach several hundreds of Kelvin.

3.3. Time evolution of disk, stellar, and envelope masses

Integrated disk and envelope masses can also give us an insight into the rate at which protostellar disks evolve with time. The left column in Figure 5 presents the stellar mass M_* (solid lines), disk mass M_d (dashed lines), envelope mass M_{env} (dash-dotted lines), and also the disk-to-star mass ratio ξ (thick solid lines) as a function of time passed since the onset of cloud core collapse. The right column shows the disk outer radius r_d . The top row corresponds to model 1, while the middle and bottom rows show the data for model 2 and model 3, respectively. The vertical dotted lines mark the onset of the Class I (left) and Class II (right) phases, which are determined using a classification breakdown of André et al. (1993) based on the mass remaining in the envelope (see Vorobyov 2010, for details). Note that the masses and disk-to-star mass ratios in the left column are plotted at different scales.

The evolution of the disk-to-star mass ratio is most illustrative of changes occurring in protostellar disks with time. Soon after the disk formation in the Class 0 or early Class I phase⁷, ξ quickly reaches a maximum value and

⁷ In fact, our disks form somewhat later than in the reality due to the use of the sink cell in our numerical simulations. However, the difference in the formation times is only of order unity.

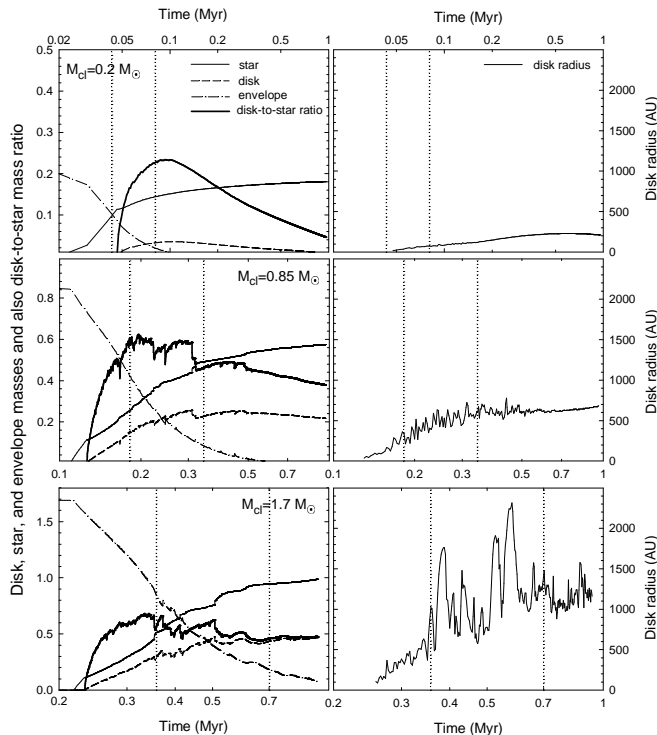


FIG. 5.— **Left column.** Time evolution of the star mass (solid lines), disk mass (dashed lines), envelope mass (dash-dotted lines), and disk-to-star mass ratio (thick solid lines) in model 1 (top), model 2 (middle), and model 3 (bottom). **Right column.** Time evolution of the disk radius r_d (solid lines) in model 1 (top), model 2 (middle), and model 3 (bottom). Vertical dotted lines mark the onset of the Class I phase (left lines) and Class II phase (right lines).

then gradually declines with time. The peak disk-to-star mass ratio in model 1 is notably smaller ($\xi \lesssim 0.25$) than in model 2 ($\xi \lesssim 0.6$) and model 3 ($\xi \lesssim 0.7$). Higher ξ favour gravitational instability and disk fragmentation, as reflected in disk images of Figure 1.

It is evident that ξ declines with time much faster in model 1 than in model 2 and 3, reflecting a progressively faster loss of disk material in lower- M_{cl} models due to accretion onto the star and, to a lesser extent, due to viscous expansion of the disk outer regions. This effect, however, is a consequence of the initial conditions. The surface density of our initial cores (see Equation 10) is close to the integrated column density of Bonnor-Ebert spheres with similar form ($r_{out}/r_0 = 6$) and density enhancement ($A = 1.2$), which implies that the low-mass cores are characterized by smaller sizes and higher densities than their high-mass counterparts (see Table 1). Such low-mass cores empty their mass reservoir faster, as seen from the time behaviour of the envelope mass in Figure 5 and can be deduced from simple free-fall-time arguments. This, in turn, means that disks in higher- M_{cl} models are replenished with the envelope material for a longer time, leading to a slower decline in ξ . The situation could be reversed if we had formed more massive cores by taking a greater positive density enhancement A but keeping the core size (r_{out}) and form fixed. In this case, more massive cores are expected to empty their mass reservoirs faster due to a higher infall rate onto the disk (e.g. Kratter et al. 2010a).

Another interesting feature, related to the disk physics rather than to the initial core setup, is that the disk

mass is steadily growing during the Class 0 phase and, to a lesser extent, in the Class I phase and shows a trend for decline only in the Class II phase. This implies that the rate of mass transport of matter from the disk outer regions onto the star is smaller than the rate of mass loading onto the disk from the infalling envelope (see also Vorobyov 2009a; Boley 2009; Kratter et al. 2010a). This phenomenon appears to be a necessary but not sufficient condition for disk fragmentation and development of the burst mode of accretion (Vorobyov & Basu 2010b). Other factors such as insufficiently large disk radii and masses may suppress disk fragmentation in low- M_{cl} models, as found in many previous studies (e.g. Matzner & Levin 2005; Rafikov 2005; Kratter et al. 2010b), even if the rate of mass infall onto the disk is higher than the rate of mass accretion onto the star.

The time evolution of the stellar mass in the intermediate and upper- M_{cl} models shows episodes of (almost) instantaneous increase, which are a manifestation of the accretion burst phenomenon (note that the disk mass shows correlated drops). Such episodes are not present in the low- M_{cl} model. The physical significance of such sharp increases in stellar mass for the early stellar evolution remains to be understood.

The time evolution of the disk radius r_d (right column in Figure 5) reveals significant differences in models with distinct cloud core masses. In the $M_{cl} = 0.2 M_{\odot}$ model 1, the disk radius steadily increases with time, reaches a maximum of $r_d = 240$ AU at $t \approx 0.5$ Myr and appears to gradually decline afterward, reflecting the ongoing stellar accretion and disk viscous dispersal. Most of the disk growth occurs in the early Class II phase due to viscous expansion. On the other hand, the disk in model 2 ($M_{cl} = 0.85 M_{\odot}$) and, especially, in model 3 ($M_{cl} = 1.7 M_{\odot}$) shows large scale radial pulsations, which are particularly strong in the Class I and early Class II phases.

These episodes of disk expansion and contraction are byproducts of the burst mode of accretion (Vorobyov & Basu 2005, 2006, 2010b). When a fragment forms in the disk via fragmentation of dense and cold spiral arms, it is quickly driven onto the star via exchange of angular momentum with the arms. This fast migration produces a transient episode of disk expansion due to conservation of angular momentum⁸, which is followed by disk contraction. Such disk pulsations pursue as long as the disk is capable of fragmenting and are usually terminated soon after the Class II phase ensues and the mass loading from the envelope diminishes. The $M_{cl} = 0.2$ model 1 is stable against fragmentation (see Figure 1) and this explains why we do not see large scale disk pulsations in this model.

Disk radial pulsations may be of great significance for the giant planet formation mechanism via direct gravitational instability. Disk contraction leads to a transient episode of density increase, during which the disk may give birth to a set of protoplanetary embryos. Most of

⁸ Globally, angular momentum of the disk plus envelope system is not conserved since we use the sink cell through which angular momentum is carried away from the system by means of protostellar jets. However, mathematically, the total angular momentum (both that of the system and that of the sink cell) is conserved, see tests in Vorobyov & Basu (2006).

them would not survive through the EPSF and are either driven onto the star or dispersed. However, when mass loading from the natal cloud core diminishes and the main fragmentation phase ends, the final disk contraction may give birth to a last and survivable set of gas giants on wide and relatively stable orbits (Vorobyov & Basu 2010a).

4. DISK STRUCTURE AND EVOLUTION ALONG THE LINE OF INCREASING CLOUD CORE ROTATION RATES

In this section, we study the structure and time evolution of protostellar disks formed via the gravitational collapse of cloud cores characterized by distinct rotational energies. For this purpose, we consider three cloud cores with the ratio of the rotational to gravitational energy $\beta = 2.8 \times 10^{-3}$ (model 4), $\beta = 5.6 \times 10^{-3}$ (model 2), and $\beta = 2.3 \times 10^{-2}$ (model 5). The ratio β is varied by increasing the rotational energy E_{rot} , while the other model parameters, in particular the cloud core masses, are kept identical.

Figure 6 presents images of the gas surface density (in g cm^{-2} , log units) for model 4 (top row), model 2 (middle row), and model 5 (bottom row). The vertical columns from left to right correspond to three distinct evolution times since the disk formation: $t = 0.1$ Myr, $t = 0.3$ Myr, and $t = 0.5$ Myr. The meaning of arrows and yellow contour lines is the same as in Figure 1. We note the spatial scale increases from 800×800 AU for models 4 and 2 to 1800×1800 AU (at $t = 0.1$ Myr and $t = 0.3$ Myr) and 5000×5000 AU (at $t = 0.5$ Myr) for model 5.

Figure 6 reveals similarities and also remarkable differences in the time evolution of protostellar disks formed from cloud cores of distinct β . While protostellar disks in all three models exhibit gravitational instability, which is strongest in the early evolution but notably weakens with time, only the $\beta = 2.3 \times 10^{-2}$ model 5 shows vigorous disk fragmentation, with some of the fragments having survived to the late evolution stage. The other two models with lower values of β experienced disk fragmentation only in the very early stage ($t \lesssim 0.1$ Myr, upper-left and upper-middle panels). However, the fragments did not survive, being either dispersed due to insufficient mass and/or numerical resolution or accreted onto the central star. By $t = 0.5$ Myr, the high- β model 5 appears to have formed a binary (or triple?) system, with masses of the primary and secondary being $0.45 M_{\odot}$ and $0.1 M_{\odot}$, respectively. In fact, the latter value is an upper limit on both the secondary companion and its disk and the companion itself may end up as an upper-mass brown dwarf. The separation between the primary and secondary was about 400 AU in the 0.3-Myr-old disk and it has increased by an order of magnitude in the 0.5-Myr-old disk, implying that the system may eventually break up and give birth to a rogue upper-mass brown dwarf. Figures 1 and 6 demonstrate that binary/multiple systems with *low* mass ratios can form as a result of *disk* fragmentation and possible progenitors are cloud cores of sufficiently high original mass *and/or* sufficiently high rotation energy. The latter requirement for disk fragmentation was also reported by Rice et al. (2010). High- β cores seem to form binaries/multiples at a notably larger spatial separation.

Our present and previous numerical simulations (Vorobyov & Basu 2006, 2010b) reveal that most frag-

ments migrate radially inward and (possibly) onto the star, while only a few migrate outward. Fragments migrate preferentially inward because they form within spiral arms and lose their angular momentum via gravitational interaction with part of the arm located at a larger radial distance. In turn, this element of the arm experiences a positive torque and moves outward (see figure 5 in Vorobyov & Basu (2006) and animation at www.astro.uwo.ca/~vorobyov). Even if a fragment forms at the very end of the arm, a continuing infall of the envelope material exerts a negative torque on this fragment, driving it radially inward. This means that only those fragments that form near the disk outer edge and in the final stages of the EPSF (when infall from the envelope diminishes) may ultimately survive and either slowly migrate outward (bottom row in Figure 6) or stabilize on orbits of order 100 AU (Vorobyov & Basu 2010a).

The growing susceptibility of protostellar disks to fragmentation along the line of increasing β can be explained by the fact that the higher- β cores form disks of larger size and greater disk-to-star mass ratio ξ . Both effects are mostly caused by the associated increase in the centrifugal radius $r_{\text{cf}} = \Omega^2 r^4 / GM(r)$ of a gas layer originally located at the radial distance r from the center. In particular, the effect of disk radius on fragmentation has been addressed by many authors (e.g. Rafikov 2005; Matzner & Levin 2005; Kratter et al. 2010b; Vorobyov & Basu 2010b) who have found that fragmentation is suppressed in small-size disks due to either stellar irradiation or viscous heating.

The left column in Figure 7 presents the time evolution of disk masses (dashed lines), stellar masses (solid lines), envelope masses (dash-dotted lines), and disk-to-star mass ratios (thick solid lines), while the right column shows the time evolution of disk radii (solid lines). In particular, the top row presents the data for the $\beta = 2.8 \times 10^{-3}$ model 4, while the middle and bottom rows correspond to the $\beta = 5.6 \times 10^{-3}$ model 2 and $\beta = 2.3 \times 10^{-2}$ model 5, respectively. The vertical dotted lines mark the onset of the Class I (left) and Class II phases (right) in each model.

In all three models, the disk-to-star mass ratio ξ quickly grows with time in the Class 0 phase, attains a maximum value in the late Class 0 or early Class I phase, and declines steadily afterwards. In the low- and intermediate- β models, the disk mass is always lower than that of the central star, with maximum $\xi = 0.5$ (model 4) and $\xi = 0.6$ (model 2). On the other hand, the disk mass in the high- β model 5 exceeds episodically that of the star in the Class I phase but drops quickly to $\xi \lesssim 0.4$ in the subsequent evolution when the binary system starts to emerge. This suggests that protostellar disks with mass comparable to or greater than that of the host star must be statistically rare and this phenomenon quickly resolves into a binary/multiple system. A similar effect was reported in numerical hydrodynamics simulations of Kratter et al. (2010a). Moreover, such massive disks must be difficult to observe due to the obscuration of light by natal envelopes that are still of substantial mass in the Class I phase. Protostellar disks formed from higher- β cores undergo radial pulsations of a notably greater amplitude. This increase is caused by a growing strength of gravitational instability and frag-

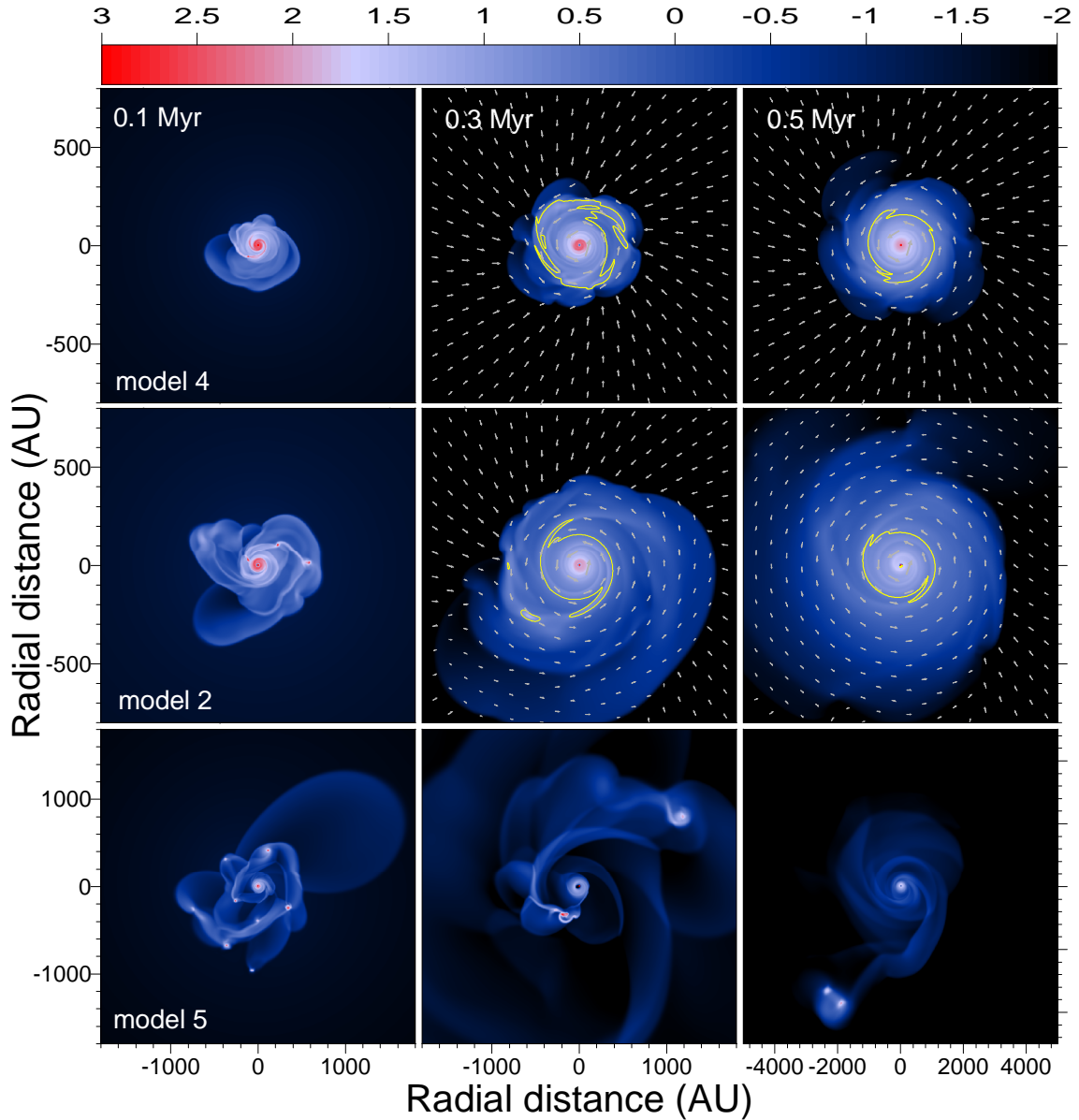


FIG. 6.— Gas surface density (in g cm^{-2} , log units) in three models with distinct ratios of the rotational to gravitational energy β and at distinct times t after the disk formation. In particular, the top row shows disk images in the $\beta = 2.8 \times 10^{-3}$ model 4, while the middle and bottom rows present those of the $\beta = 5.6 \times 10^{-3}$ model 2 and $\beta = 2.3 \times 10^{-2}$ model 5, respectively. Columns from left to right correspond to $t = 0.1$ Myr, $t = 0.3$ Myr, and $t = 0.5$ Myr, respectively. Superimposed on the disk images are the gas velocity fields (arrows) and yellow contour lines delineating disk regions with the frequency-integrated optical depth $\tau \geq 0.1$.

mentation. In all three models, the radial pulsations appear to subside with time.

Finally, in Figure 8 we consider the azimuthally-averaged radial profiles (from top to bottom row) of the gas surface density, midplane gas temperature, optical depth, integrated mass, and angular velocity at $t = 0.1$ Myr (left column), $t = 0.3$ Myr (middle column), and $t = 0.5$ Myr (right column) after the disk formation. In particular, the solid, dashed and dash-dotted lines correspond to model 4, model 2, and model 5, respectively. The meaning of the dotted lines is the same as in Figure 3.

A visual inspection of Figure 8 reveals that protostellar disks formed from cloud cores of increasingly higher β are characterized by *lower* azimuthally-averaged gas surface density $\bar{\Sigma}$, midplane temperature \bar{T} , and optical depth $\bar{\tau}$. At the same time, both the disk size and mass in-

crease along the line of increasing β . Lower $\bar{\Sigma}$ do not prevent higher- β disks from fragmenting, as Figure 6 demonstrates. On the contrary, these disks are more susceptible to fragmentation, owing to their larger size and lower gas temperature. The latter effect is caused by lower stellar irradiation fluxes at larger radii and lower viscous heating (e.g. Matzner & Levin 2005; Kratter et al. 2010b). A substantial fraction of protostellar disks in the low- and intermediate- β models 4 and 2 are optically thick, suggesting that the mass of such disks may be systematically underestimated using conventional observational techniques. Sharp jumps in the integrated mass of model 5 at 400 AU (0.1-Myr-old disk), 1200 AU (0.3-Myr-old disk), and 4200 AU (0.5-Myr-old disk) reflect the formation and outward drift of a sub-stellar companion.

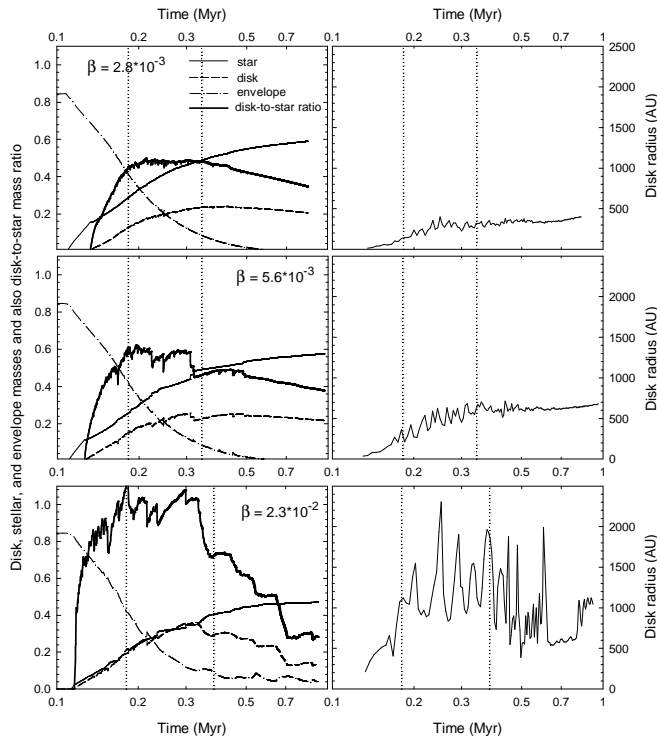


FIG. 7.— **Left column.** Time evolution of the star mass (solid lines), disk mass (dashed lines), envelope mass (dash-dotted lines), and disk-to-star mass ratio (thick solid lines) in model 4 (top), model 2 (middle), and model 5 (bottom). **Right column.** Time evolution of the disk radius r_d (solid lines) in model 4 (top), model 2 (middle), and model 5 (bottom). Vertical dotted lines mark the onset of the Class I phase (left lines) and Class II phase (right lines).

5. CONCLUSIONS

Using numerical hydrodynamics simulations in the thin-disk approximation, we model the formation and evolution of protostellar disks in the embedded phase of star formation when the disks are exposed to intense mass loading from natal cloud cores and are difficult to probe using conventional observational techniques. The key physical processes that are taken into consideration in our modeling include: disk self-gravity, viscous and shock heating, stellar and background irradiation, radiative cooling from the disk surface, and also self-consistent accretion of gas from the disk onto the forming star and from the infalling envelope onto the disk. We scrutinize the structure and time evolution of protostellar disks formed from five model cloud cores with distinct initial masses in the $0.2\text{--}1.7 M_\odot$ range and ratios of the rotational to gravitational energy β in the $0.28\text{--}2.3 \times 10^{-2}$ range. We find the following.

- The time evolution of embedded protostellar disks proceeds from a conspicuously non-axisymmetric state toward a more regular, axisymmetric appearance. Simultaneously, the gas surface density reduces and disks expand radially outward with time. However, the time scale for this transformation is faster in lower-mass disks formed from cloud cores of smaller mass. For instance, disks formed from cloud cores of $M_{cl} = 0.2 M_\odot$ are virtually axisymmetric at $t = 0.3$ Myr after their formation, while more massive disks formed from cloud cores of $M = 0.85 M_\odot$ retain a notable diffuse spiral

structure at $t = 0.5$ Myr. In the non-axisymmetric state, massive disks are often lopsided and the gas flow exhibits non-circular motions, indicating local deviations from a circular rotation caused by spiral arms and forming fragments.

- Disk fragmentation is seen in most models. However, most of the fragments do not survive through the embedded phase and are either destroyed or driven onto the forming star. Only models with sufficiently high M_{cl} or β (for instance, $M_{cl} = 1.7 M_\odot$ and $\beta = 5.6 \times 10^{-3}$ or $M_{cl} = 0.85 M_\odot$ and $\beta = 2.3 \times 10^{-2}$) reveal the formation of wide-separation binary/multiple systems with low mass ratios and (possibly) brown dwarf companions. In particular, systems formed from cloud cores with $\beta \gtrsim 2.3 \times 10^{-2}$ may ultimately break up, delivering freely wandering brown dwarfs to the natal star forming region. These rogue brown dwarfs may even possess some minidisks, the properties of which remain to be studied.
- The fact that only sufficiently massive cores with sufficiently high initial rotational energy E_{rot} form binary systems can in part account for a lower binary fraction found in stars of lower mass. Low-mass stars tend to form from low-mass cores and only a small fraction of these cores with high enough E_{rot} can give birth to a binary system. As the core mass grows (and so does the resulting mass of the star), more and more cores can form binary systems because the requirement of sufficiently high initial rotational energy is relaxed along the line of increasing core mass.
- Embedded protostellar disks of *equal* age formed from cloud cores of greater mass (but equal β) are generally characterized by higher gas surface densities, higher midplane temperatures, larger radii, and greater masses. On the other hand, protostellar disks formed from cloud cores of higher β (but equal M_{cl}) are generally thinner and colder but larger and more massive.
- The trend of more massive cloud cores to form denser and hotter disks diminishes for $M_{cl} \gtrsim 0.9 M_\odot$ owing to the onset of vigorous gravitational instability and fragmentation. Gravitational torques efficiently transport matter in the form of fragments from the disk outer regions (where most of the envelope material lands and fragmentation takes place) onto the star, preventing the disk from growing in density and bringing it back to the border of stability. However, the disk continues to grow in size (and mass) due to infall of the envelope material with high angular momentum (which may lead to another fragmentation episode). This process continues until the envelope is depleted of matter.
- The positive difference between the midplane and irradiation temperatures is significant only in the inner disk regions ($r \lesssim 50$ AU), near the disk's outer edge and dense fragments, where it can reach a factor of two or more. The degree of vertical

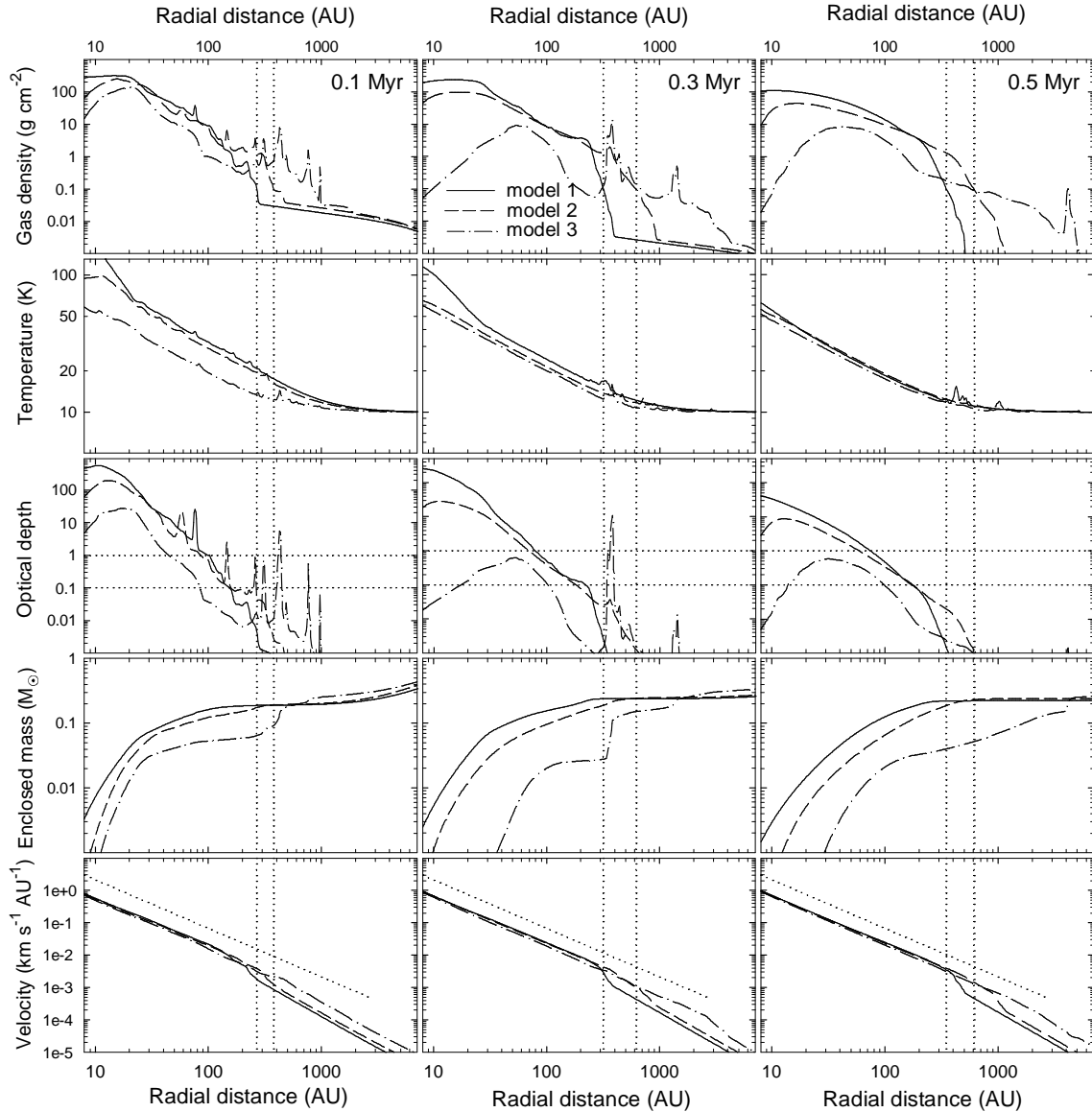


FIG. 8.— Azimuthally-averaged radial profiles of the gas surface density $\bar{\Sigma}$ (first row), gas midplane temperature \bar{T} (second row), frequency-integrated optical depth $\bar{\tau}$ (third row), and angular velocity $\bar{\Omega}$ (fifth row). The fourth row presents the enclosed mass $M(r)$ as a function of radius. The vertical columns from left to right show the data at three different times after the disk formation: $t=0.1$ Myr (left), $t=0.3$ Myr (middle), and $t=0.5$ Myr (right). The solid, dashed, and dash-dotted lines present the data for the $\beta = 2.8 \times 10^{-3}$ model 4, $\beta = 5.6 \times 10^{-3}$ model 2, and $\beta = 2.3 \times 10^{-2}$ model 5, respectively. The vertical dotted lines mark the position of the disk outer edge in model 4 (left lines) and model 2 (right lines). The meaning of other dotted lines is the same as in Figure 1.

non-isothermality becomes progressively smaller in disks formed from cloud cores of smaller mass and as the disks evolve.

- Protostellar disks in the embedded phase (especially in the Class I phase) show radial pulsations, the amplitude of which increases along the line of increasing M_{cl} and β . These pulsations are caused by gravitational instability and, to a greater extent, by disk fragmentation and accretion of fragments onto the protostar. The amplitude of radial pulsations appears to diminish in the Class II phase when the envelope clears.
- The disk-to-star mass ratio ξ increases along the line of increasing M_{cl} and/or β . A maximum value of β of order unity is achieved in single stars formed from cloud cores with high rates of rotation $\beta \gtrsim$

2.3×10^{-2} . However, such massive disks are short-lived and by the end of the embedded phase they quickly evolve into a binary/multiple system.

- A substantial fraction of a protostellar disk in the embedded phase may be optically thick, implying that observationally inferred disk masses may be underestimated.

We also provide useful approximation formula to the radial profiles of the gas surface density and midplane temperature at different stages of the evolution and for disks of different mass. We did not see the formation of planetary-mass objects in protostellar disks as in numerical simulations with a barotropic equation of state by Vorobyov & Basu (2010a). However, we hope to see them forming in our future simulations because some of our low-mass fragments seem to disperse due to the lack

of numerical resolution at large radii where our logarithmic grid diverges. Finally, it is worth noting that the results may be somewhat dependent on the chosen angular momentum and density profiles. We plan to vary the initial profiles in a future study.

The author is thankful to the anonymous referee for useful comments and suggestions that helped to improve the paper. The author gratefully acknowledges present

support from an ACEnet Fellowship. Numerical simulations were done on the Atlantic Computational Excellence Network (ACEnet), on the Shared Hierarchical Academic Research Computing Network (SHARCNET), and at the Center of Collective Supercomputer Resources, Taganrog Technological Institute at Southern Federal University. This project was also supported by RFBR grant 10-02-00278 and by Ministry of Education grant RNP 2.1.1/1937.

REFERENCES

- Akeson, R. L., Ciardi, D. R., van Belle, G. T., & Creech-eakman, M. J. 2002, *ApJ*, 566, 1124
- André, P., Ward-Thompson, D., & Barsony, M. 1993, *ApJ*, 406, 122
- Andrews, S. M., & Williams, J. P. 2005, *ApJ*, 631, 1134
- Andrews, S. M., & Williams, J. P. 2007, *ApJ*, 659, 705
- Andrews, S. M., Wilner, D. J., Huges, A. M., Qi, C., & Dullemond, C. P. 2009, *ApJ*, 700, 1502
- Baraffe, I., Chabrier, G., & Gallardo, J. 2009, *ApJL*, 702, 27
- Basu, S. 1997, *ApJ*, 485, 240
- Bate, M. R., Bonnell, I. a., & Bromm, V. 2003, *MNRAS*, 339, 577
- Beckwith, S. V. W., Sargent, A. I., Chini, R. S., & Guesten, R. 1990, *AJ*, 99, 924
- Bell, K. R., & Lin, D. N. C. 1994, *ApJ*, 427, 987
- Boley, A. C. 2009, *ApJL*, 695, 53
- Boley, A. C., Hayfield, T., Mayer, L., & Durisen, R. H. 2009, *astro-ph:0909.4543*
- Boss, A. P. 1998, *ApJL*, 501, 77
- Boss, A. P., & Hartmann, L. W. 2001, *ApJ*, 562, 842
- Brown, D. W., et al. 2000, *MNRAS*, 319, 154
- Burkert, A., Bate, M. R., Bodenheimer, P. 1997, *MNRAS*, 289, 497
- Caselli, P., Benson, P. J., Myers, P. C., & Tafalla, M. 2002, 572, 238
- Clarke, C. J. 2009, *MNRAS*, 396, 1066
- D'Alessio, P., Calvet, N., Hartmann, L., Lizano, S., & Canto, J. 1999, *ApJ*, 527, 893
- D'Antona, F., & Mazitelli, I. 1997, *Memorie della Societa Astronomia Italiana*, 68, 807
- Dunham, M. M., Evans II, N. J., Terebey, S., Dullemond, C. P., Young, C. H. 2010, *ApJ*, 710, 470
- Evans II, N. J., Dunham, M. M., Jorgensen, J. K., Enoch, M. L., Merín, B., van Dishoeck, E. F., et al. *ApJSS*, 181, 321
- Eisner, J. A., Hillenbrand, L. A., & Carpenter, J. M. 2005, *ApJ*, 635, 396
- Eisner, J. A., Plambeck, R. L., Carpenter, J. M., Corder, S. A., Qi, C., & Wilner, D. 2008, *ApJ*, 683, 304
- Enoch, M. L., Evans, N. J., II, Sargent, A. I., & Glenn, J. 2009, *ApJ*, 692, 973
- Hartmann, L., Calvet, N., Gullbring, E., & D'Alessio, P. 1998, *ApJ*, 495, 385
- Hollenbach, D. J., Yorke, H. W., & Johnstone, D. 2000, in *Protostars and Planets IV*, ed. V. Mannings, A. P. Boss, & S. S. Russell (University of Arizona Press), 401
- Hueso, R., & Guillot, T. 2005, *A&A*, 442, 703
- Johnson, B. M. & Gammie, C. F. 2003, *ApJ*, 597, 131
- Ida, S., & Lin, D. N. C. 2004, *ApJ*, 604, 388
- Isella, A., Carpenter, J. M., & Sargent, A. I. 2009, *ApJ*, 701, 260
- Johnson, B. M. & Gammie, C. F. 2003, *ApJ*, 597, 131
- Laughlin, G., Bodenheimer, P. 1994, *ApJ*, 436, 335
- Jørgensen, J. K., van Dishoeck, E. F., Visser, R., Bourke, T. L., Wilner, D. J., Lommen, D., Hogerheijde, M. R., & Myers, P. C. 2009, *A&A*, 507, 861
- Looney, L. W., Mundy, L. G., Welch, W. J. 2003, *ApJ*, 592, 255
- Kitamura, Y., Momose, M., Yokogawa, S., Kawabe, R., Tamura, M., & Ida, S. 2002, *ApJ*, 581, 357
- Kratter, K. M., Matzner, C. D., & Krumholz, M. R. 2008, *ApJ*, 681, 375
- Kratter, K. M., Matzner, C. D., Krumholz, M. R., & Klein, R. I. 2010a, *ApJ*, 708, 1585
- Kratter, K. M., Murray-Clay, R. A., Youdin, A. N. 2010b, *ApJ*, 710, 1375
- Krumholz, M., & Burkert, A. 2010, *astro-ph:1003.4513*
- Krumholz, M. R., Klein, . I., & McKee, F. C. 2007, *ApJ*, 656, 959
- Lin, D. N. C., & Pringle, J. E. 1990, 358, 515
- Lodato, G., Rice, W. K. M. 2005, *MNRAS*, 358, 1489
- Luaghlin, G., Bodenheimer, P. 1994, *ApJ*, 436, 335
- Machida, M. N., Inutsuka, S., Matsumoto, T. 2010, *astro-ph:1001.1404*
- Mannings, V., & Sargent, A. I. 2000, *ApJ*, 529, 391
- Masunaga, H., & Inutsuka, S. 2000, *ApJ*, 531, 350
- Matzner, D. C., & Levin, Yu. 2005, *ApJ*, 628, 817
- Nakamoto, T., & Nakagawa, Y. 1994, *ApJ*, 421, 640
- Natta, A., Grinin, V. P., & Mannings, V. 2001, in *Protostars and Planets IV*, ed. V. Mannings, A. P. Boss, & S. S. Russell (Tucson, AZ: Univ. Arizona Press), 559
- Nelson, A. F., Benz, W., & Ruzmaikina, T. V. 2000, *ApJ*, 529, 357
- Palla, F., & Stahler, S. W. 1991, *ApJ*, 375, 288
- Pickett, B. K., Cassen, P., Durisen, R. H., & Link, R. 2000, *ApJ*, 529, 1034
- Piétu, V., Dutrey, A., & Guilloteau, S. 2007, *A&A*, 467, 163
- Pollack, J. B., Hubickyj, O., Bodenheimer, P., Lissauer, J. J., Podolak, M., & Greenzweig, Y. 1996, *Icarus*, 124, 62
- Rafikov, R. R. 2005, *ApJ*, 621, L69
- Rice, W. K. M., Mayo, J. H., & Armitage, P. J. 2010, *MNRAS*, 402, 1740
- Richtmyer, R. D., & Morton, K. W. 1957, *Difference Methods for Initial-Value Problems*, 2d ed. (New York: Wiley Interscience)
- Vicente, S. M., & Alves, J. 2005, *A&A*, 441, 195
- Visser, R. van Dishoeck, E. F., Doty, S. D. & Dullemond, C. P. 2009, *A&A*, 495, 881
- Vorobyov, E. I., & Basu, S. 2005, *ApJL*, 633, 137
- Vorobyov, E. I., & Basu, S. 2006, *ApJ*, 650, 956
- Vorobyov, E. I., 2009a, *ApJ*, 692, 1609
- Vorobyov, E. I. 2009b, *ApJ*, 704, 715
- Vorobyov, E. I., & Basu, S. 2009a, *ApJ*, 703, 922
- Vorobyov, E. I., & Basu, S. 2009b, *MNRAS*, 393, 822
- Vorobyov, E. I. 2010, *ApJ*, 713, 1
- Vorobyov, E. I., & Basu, 2010a, *ApJL*, 714, 133
- Vorobyov, E. I., & Basu, S. 2010b, *ApJ*, 719, 1896
- Wiebe, D. S., Semenov, D. A., Henning, T. 2008, *Astronomy Reports*, 52, 941
- Wild, W. et al. 2009, *Exp Astron*, 23, 221
- Yorke, H. W., & Bodenheimer, P. 1999, *ApJ*, 525, 330
- Zhu, Z., Hartmann, L., Gammie, C. McKinney, J. C. 2009, *ApJ*, 701, 620